PHYSICAL REVIEW A **96**, 021401(R) (2017)

Time-resolved measurement of internal conversion dynamics in strong-field molecular ionization

Vincent Tagliamonti,[1] Brian Kaufman,[1] Arthur Zhao,[1] Tamás Rozgonyi,[2] Philipp Marquetand,[3] and Thomas Weinacht[1]

[1]*Department of Physics and Astronomy, Stony Brook University, Stony Brook, New York 11794-3800, USA* [2]*Institute of Materials and Environmental Chemistry, Research Centre for Natural Sciences, HAS, Budapest 1117 Magyar tudósok krt. 2, Hungary*

[3]*University of Vienna, Faculty of Chemistry, Institute of Theoretical Chemistry, Währinger Straße 17, 1090 Wien, Austria*

(Received 31 May 2017; published 2 August 2017)

We time-resolve coupled electronic and nuclear dynamics during strong-field molecular ionization by measuring the momentum-resolved photoelectron yield as a function of pump-probe delay for a pair of strong-field laser pulses. The sub-10-fs pulses are generated using a specially designed ultrafast optical pulse shaper and the electrons are measured using velocity map imaging. Our measurements, in conjunction with calculations that solve the time-dependent Schrödinger equation, allow us to time-resolve resonance-enhanced strong-field ionization and break it down into three basic steps: (1) Stark-shifted resonant excitation of a high-lying neutral state of the molecule, (2) nonadiabatic dynamics (internal conversion) in which multiple electronic states are coupled, and (3) coupling to the continuum (ionization)

I. INTRODUCTION AND BACKGROUND

Strong-field atomic ionization plays a crucial part in high-harmonic generation as well as the production of attosecond pulses [1–5]. In recent years, strong-field molecular ionization has drawn significant interest as a probe of molecular structure and dynamics [6–9]. In both cases, excited states of the system can be Stark shifted into resonance by the strong field of the laser pulse, leading to significant enhancement of the ionization yield [10–16]. While resonance-enhanced ionization involves only electronic dynamics in atomic systems, it is more complicated in molecules due to the possibility for coupled electronic and nuclear dynamics and a breakdown of the Born-Oppenheimer approximation [17–21]. Time-resolved photoelectron spectroscopy (TRPES) provides detailed information about these nonadiabatic dynamics because the photoelectron spectrum identifies the ionic state, which is correlated with the neutral state on which the wave function is evolving. The work presented here serves as a bridge connecting strong-field molecular ionization with TRPES [22, 23].

In our previous work studying CH_2IBr, we found that vibrational dynamics and nonadiabatic transitions following resonant excitation of the neutral molecule could be suppressed by using laser pulses with a duration shorter than the vibrational period [24]. By making the pulses sufficiently short (<10 fs), we were able to "freeze-out" the nuclear motion, preventing population transfer via nonadiabatic coupling, resulting in ionization to only a single state of the cation. For longer pulses, the nonadiabatic coupling between neutral excited states led to internal conversion during the ionization dynamics, resulting in the population of multiple cationic states, each of which was Dyson-correlated [25] with a specific excited neutral state of the molecule [26–28]. However, if the pulse duration was comparable to or longer than a vibrational period (>20 fs), internal conversion and ionization could occur during the laser pulse but could not be time resolved and separated.

In order to facilitate a discussion of the dynamics addressed in this work, we consider a simplified picture based on the potential energy curves of the neutral shown in Fig. 1. (R_1), correlated with the first excited state of the cation (D_1), comes into resonance during the laser pulse. The reaction coordinate in this picture is the CH_2 wagging mode, the only mode for which there is both significant displacement of excited-state minima from the Franck-Condon (FC) point and crossings between states, facilitating nonadiabatic transitions. As discussed above, probing the dynamics with ionization by a short laser pulse (<10 fs) would then suppress nonadiabatic transitions and lead to the population of a single ionic state D_1, with a single peak in the photoelectron spectrum (top inset of Fig. 1). Ionization of the wave packet at later times leaves time for nonadiabatic transitions to other electronic states (R_1 to R_3 at C_1 followed by R_3 to R_0 at point C_2). The electronic states R_3 and R_0 are correlated with states D_3 and D_0 of the cation, respectively, and thus the nonadiabatic dynamics in the neutral molecule can lead to the population of multiple states of the cation as the population in R_3 and R_0 is ionized (middle and bottom insets of Fig. 1).

The previous results and the picture described above indicate that the wave packet dynamics involve nonadiabatic coupling and internal conversion in a fraction of the vibrational period. Now, we use pump-probe spectroscopy to not only gain access to this time scale, but also to decouple the excitation and ionization. We explicitly follow these nonadiabatic dynamics with the pump-probe pulse pair, each with a duration less than 10 fs, during which vibrational dynamics are largely frozen and internal conversion is suppressed.

In this work, the pump pulse drives multiphoton excitation to the neutral excited state R_1 at the FC point and launches a vibrational wave packet since the pump pulse duration is shorter than a vibrational period of the CH_2 wagging mode. After resonant excitation, we time-resolve the coupled electronic and nuclear dynamics of the wave packet as it undergoes nonadiabatic transitions to different neutral excited states, using strong-field ionization as a probe. We measure the momentum-resolved photoelectron yield as a function of pump-probe delay, allowing us to see how the population is transferred between electronic states of the neutral molecule following excitation.

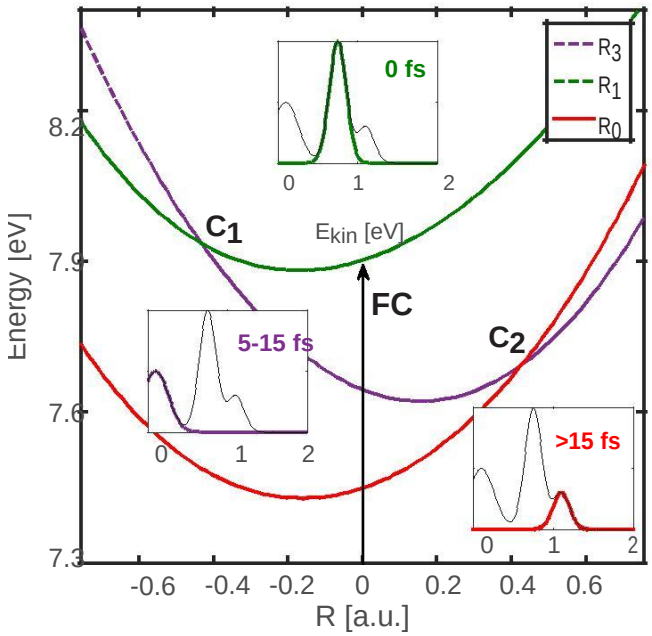

FIG. 1. One-dimensional neutral potentials along the wagging mode of CH_2 with energy measured relative to the neutral ground state. The diabatic states shown are coupled via coupling elements of Gaussian shape with a strength of 0.082 eV and a FWHM of 0.6 a.u. (see [24] for further details). The first nonadiabatic crossing, C_1, is reached in about 5 fs. The second crossing, C_2, is reached in 15–20 fs. (Insets) Cartoons of the expected photoelectron spectra due to ionization at several critical time delays are shown. The black line is the total photoelectron spectra with contributions from all ionic states integrated over time.

vibrational dynamics on the neutral excited states as well as nonadiabatic couplings [12, 24]. Dynamics in the molecular cation have been studied in earlier publications [30, 31] but are not relevant to the current study, since the photoelectron spectrum is not affected by dynamics in the cation following ionization [32].

II. EXPERIMENTAL APPARATUS

To follow the dynamics described above, we developed a broadband acousto-optic modulator (AOM)-based ultrafast optical pulse shaper to conduct time-resolved measurements of the excitation and ionization using 10-fs pump and probe pulses [33, 34]. We produce pairs of few-cycle laser pulses with control over both the amplitude and phase as well as the time delay between the pulses. An important capability of the pulse shaper is that it allows for specialized tailoring and fine control of the individual intensities of the pulses. For short time delays between the pulses, for example, temporal overlap leads to a variation of the peak intensity with delay. To investigate dynamics which are sensitive to intensity and occur on time scales comparable to the pulse duration, we maintain a nearly constant peak intensity for short time delays by adjusting the pulse amplitude at each delay (described in detail below).

To generate the shaped laser pulses, we begin with a mode-locked Ti:sapphire oscillator and use an amplifier to produce 30-fs pulses with a central wavelength of 780 nm and more than 1 mJ per pulse at a 1 kHz repetition rate. Pulses with octave-spanning bandwidth (400–900 nm at the tails) are produced through supercontinuum generation in argon gas [29, 35]. To compress the pulses and produce durations of less than 10 fs, we use an AOM-based pulse shaper in a $4f$ geometry [33, 36] and perform a multiphoton intrapulse interference phase scan (MIIPS) to retrieve the optical phase [37– 41]. Using the pulse shaper, we apply the phase correction retrieved with the MIIPS algorithm to produce compressed pulses near the Fourier transform limit.

The AOM-based pulse shaper itself consists of an antireflection-coated fused silica modulator (Brimrose) and arbitrary waveform generator (Wavepond). The AOM has a peak diffraction efficiency of ~50% for a 15-W, 7-μs pulsed rf (radio frequency) traveling acoustic wave around 150 MHz. Each of the two diffraction gratings in the shaper has an average efficiency of 50%. Typically, the pulse energy input to the shaper is 160 μJ, which produces a diffracted, compressed pulse energy of about 25 μJ. This is enough pulse energy to perform strong-field ionization experiments using several pulse parametrizations, including double pulses.

The pulses are focused inside a vacuum chamber to produce intensities of 10–15 TW/cm^2. All of the experiments are performed with a base pressure of 2×10^{-9} torr. We introduce the sample using an effusive molecular beam at room temperature with typical pressures of 1×10^{-6} torr. The laser is linearly polarized in the plane of the detector for all measurements. Upon ionization, we measure photoelectrons which are accelerated toward a dual stack of microchannel plates (MCP) and phosphor screen using a velocity map imaging (VMI) electrostatic lens.

The VMI produces a two-dimensional projection of the three-dimensional charged particle distribution which can be measured with the MCP and phosphor screen [42]. The phosphor screen fluoresces producing a two-dimensional velocity distribution of charged particles which is recorded for each laser shot at 1 kHz with a complementary metal-oxide semiconductor (CMOS) camera (Basler acA2000-340km) capable of short exposure times (24 μs). We implement a fast computer algorithm to threshold and identify the coordinates of the centroid of each detected particle for each laser shot and save only these coordinates. With this information, we construct a synthetic VMI figure which is both background and noise free and is largely free from the nonuniformity of particle detection due to the spatial gain variation of the MCP (see insets of Fig. 2). The data are then inverse-Abel transformed using the BASEX method [43], and an angular integration is performed to produce the photoelectron spectrum. Although we present only photoelectron data, this detection system is designed for both ion and electron measurements and is described in detail in Ref. [44].

III. OPTICAL MEASUREMENTS AND PULSE CHARACTERIZATION

The experiments presented in this work involve a pair of high-intensity laser pulses which are produced by applying modulation to the amplitude of the rf pulse in the frequency domain as in Eq. (1). In general, the programmed amplitude

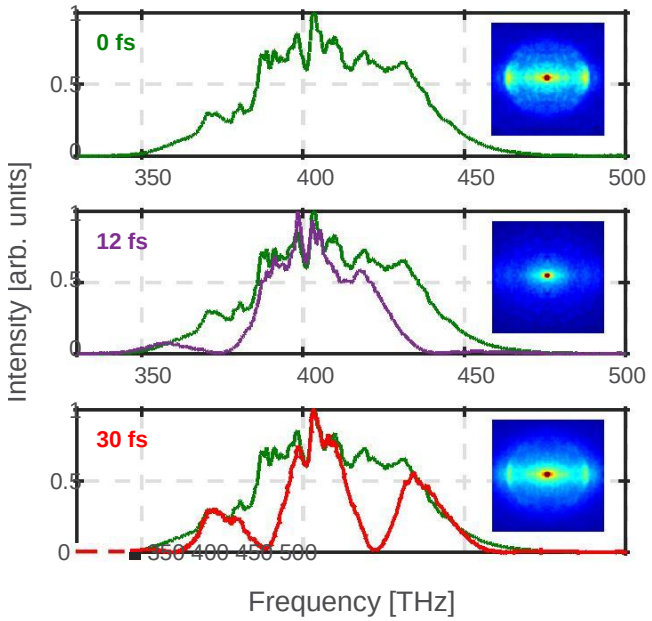

FIG. 2. Optical spectra for a pair of 10-fs pulses produced with the pulse shaper after the phase correction is applied to compensate the optical phase for three pump-probe delays. The green spectrum is for a single pulse and is shown in all plots for comparison. (Inset) Velocity map images of photoelectrons from the ionization of CH_2IBr for each pump-probe delay.http://learnrnd.com/detail.php?id=Environmental_Influences_on_the_Aging

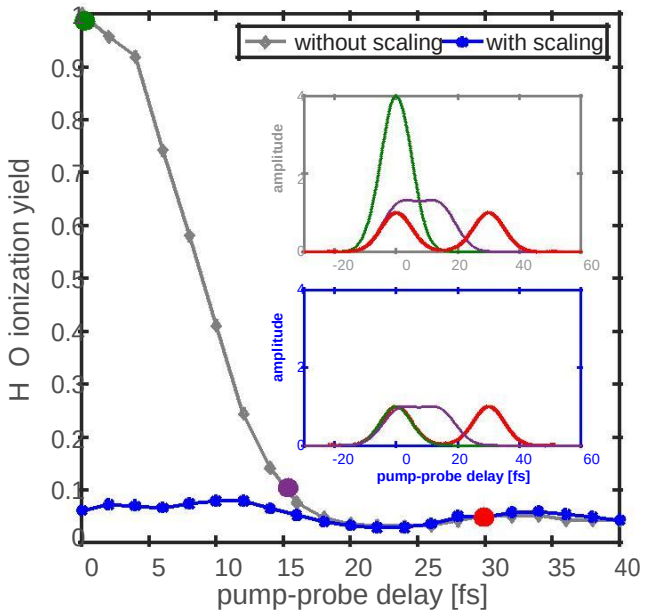

FIG. 3. Photoelectron yield for the ionization of H_2O with 10-fs pulses. The amplitude of the pulses at several delays are shown for Gaussian pulses. For two pulses each with peak amplitude 1, the peak amplitude at zero time delay is the sum of the individual pulse peak amplitudes and the intensity is $2^2 = 4$. Thus, to maintain a constant peak intensity, the total amplitude can be divided by the peak amplitude at each time delay. Insets: (Top) Double-pulse intensity profiles for two equal pulses for 0-, 15-, and 30-fs delays with no compensation (scaling factor) for the increased peak amplitude when the pulses are overlapped. (Bottom) Intensity profiles when a peak amplitude scaling factor is applied [$\sigma(\tau)$ in Eq. (1)].

and phase of the rf are mapped to optical frequency by applying a mask function specifying the parameters as a function of the acoustic travel time of the rf pulse (see [45] for a review). This provides a control over the amplitude and phase of the laser pulse in the frequency domain. The resulting laser electric field $E(\omega)_{\text{shaped}}$ is a product of the input field $E(\omega)_{\text{input}}$ and mask function $M(\omega)$ such that

$$E(\omega)_{\text{shaped}} = E(\omega)_{\text{input}} M(\omega),$$
$$M(\omega) = \sigma(\tau)[1 + a e^{-i(\omega - \omega_L)\tau}] \quad (1)$$

Here, a is the relative amplitude of the probe to the pump pulse, ω is the angular optical frequency, ω_L is the phase-locked frequency, and τ is the time delay. In this work, a = 0.8 such that the probe is 80% the amplitude of the pump. An overall amplitude scaling factor $\sigma(\tau)$ is used to control the pulse intensity as a function of pump-probe delay (described below). We keep ω_L fixed at the central frequency of the optical spectra (ω_0) such that the field at frequency ω_L interferes constructively for all pump-probe time delays.

Given that the pulse shaper can produce an identical pair of phase-locked pulses, spectral interference can be observed in the frequency domain. Figure 2 shows optical spectra for a pulse pair separated by 0-, 12-, and 30-fs delay. The double pulse spectrum shows interference fringes separated by $\delta\nu$, where ν is the optical frequency in terahertz. The time delay between the pulses τ corresponds to the inverse of the spacing between maxima or minima in the spectrum, $1/\delta\nu$. Changes in the optical spectra are accompanied by changes in the measured photoelectrons with velocity map imaging. The insets of Fig. 2 show photoelectrons from the ionization of CH_2IBr measured with VMI for several pump-probe time delays. To quantitatively compare the ionization at each time delay, the photoelectron energy spectra are calculated from the VMI data. A typical data set of photoelectron spectra vs pump-probe delay is shown in Fig. 4 and will be described in detail below.

An advantage of using the pulse shaper and applying the appropriate mask function to the pulse amplitude is that we can mitigate the variation in intensity when the pulse pair is separated by time delays less than the single-pulse duration. Pump-probe experiments using pulses of the same optical frequencies and polarizations typically suffer from optical interference near zero time delay. The pulse amplitudes are added coherently, resulting in an increase in the peak intensity while the pulses are overlapped in time. As the strong-field ionization dynamics (including the Stark-shifted resonance of R_1) are very sensitive to the intensity of the pulses, it is important to maintain a constant peak intensity for comparing measurements at different pump-probe delays. We are able to compensate for this intensity variation with an amplitude scaling function $\sigma(\tau)$ in Eq. (1). An example of this intensity compensation is shown in Fig. 3, where the photoelectron yield from the ionization of water is plotted with and without compensation (scaling). The yield is 10–20 times higher with no scaling applied in the first 10 fs when the pulses are largely overlapped. Once the scaling is applied (see inset of Fig. 3), the yield is nearly constant for short time delays where there is significant pulse overlap.

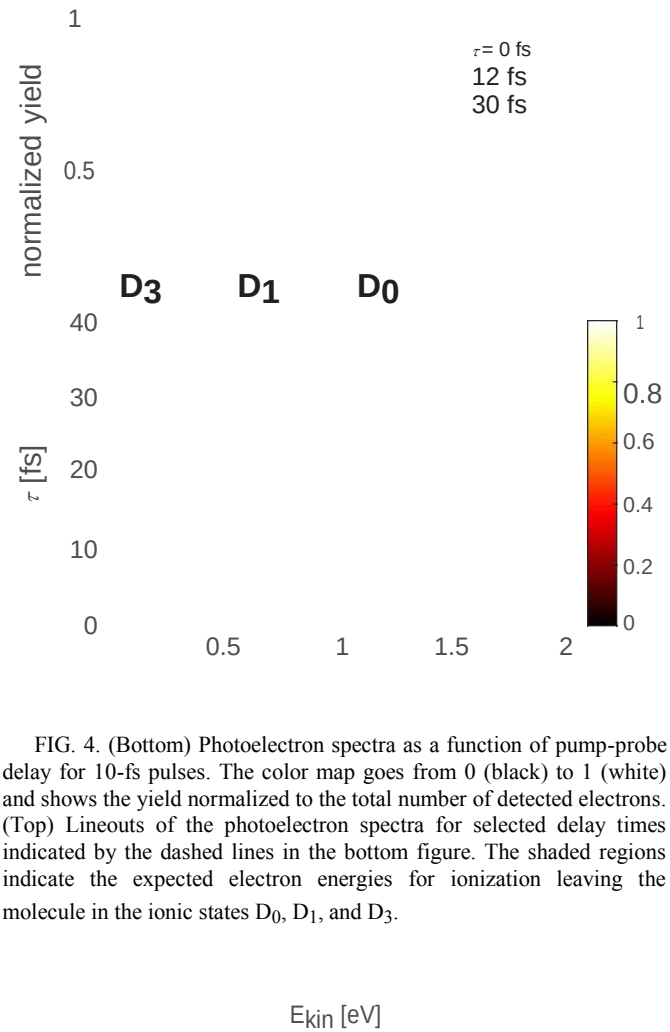

FIG. 4. (Bottom) Photoelectron spectra as a function of pump-probe delay for 10-fs pulses. The color map goes from 0 (black) to 1 (white) and shows the yield normalized to the total number of detected electrons. (Top) Lineouts of the photoelectron spectra for selected delay times indicated by the dashed lines in the bottom figure. The shaded regions indicate the expected electron energies for ionization leaving the molecule in the ionic states D_0, D_1, and D_3.

IV. EXPERIMENTAL RESULTS

Figure 4 shows the photoelectron spectra (PES) as a function of pump-probe delay for strong-field ionization of CH_2IBr with a strong-pump and weak-probe scheme. We note that while the probe pulse is weaker than the pump, neither interact with the molecules in the weak-field limit. The measurements depend on the intensity of the pump and probe pulses, but we found qualitatively similar results for intensities within 20% of the intensity used to make the measurements shown in Fig. 4. Each photoelectron spectrum in Fig. 4 is the result of a VMI measurement taken at a pump-probe delay time in 2-fs increments up to 40 fs. The PES are calculated for all electrons (all angles in the VMI) and normalized to the total number of electrons detected (total electron yield). This results in the photoelectron spectrum per electron as a function of delay.

There are three main peaks in the PES which correspond to the production of low-lying states of the cation, namely, D_0, D_1, and D_3. The neutral states R_0, R_1, and R_3 are Dyson-correlated with the low-lying ionic continua D_0, D_1, and D_3, respectively [27, 28]. The assignment of the peaks in Fig. 4 has been carried out in previous work and verified with electron-

where $h\nu$ is the photon energy of 1.66 eV, I_p is the ionization potential (9.69, 10.26, and 11.12 eV for D_0, D_1, and D_3, respectively), and U_p is the ponderomotive energy, given by $U_p = e^2 I/2\_0 m_e c\omega^2$, where I is the peak laser intensity and ω is the angular frequency of the laser. The ponderomotive potential is estimated to be approximately 0.5–0.7 eV based on previous work [24, 29]. For multiphoton ionization involving a total of $n = 7$ photons (5 + 2 given the intermediate resonance with R_1), the peaks can be assigned as D_0 at 1.1–1.2 eV, D_1 at 0.6–0.8 eV, and D_3 at 0–0.3 eV, as indicated by the shaded regions in the top of Fig. 4. The two-dimensional plot in Fig. 4 (bottom panel) shows the evolution of the ionization as a function of delay time. Lineouts of the PES at several time delays are also shown in the top panel. Near zero time delay, the dominant peak in the spectrum is D_1 at 0.8 eV, with a small contribution from D_3 and D_0. The ionization to D_3 continues to increase for delays between 5 and 15 fs. During this time, ionization to D_1 is decreased. At 12 fs, ionization to D_3 reaches a maximum and is the dominant contribution, while D_0 and D_1 are roughly equal to each other. However, as the delay time is increased beyond 15 fs, the contribution from ionization to D_3 is decreased. Around 15 fs, the ionization to D_0 begins to increase and remains for delays up to 40 fs. For longer pump-probe time delays of 30 fs or more, D_1 again becomes dominant, though the amplitude is now more comparable to both D_0 and D_3.

V. SIMULATION

In order to interpret the experimental findings and test the basic picture of the nonadiabatic dynamics outlined in Fig. 1, we model the strong-field ionization with numerical integration of the time-dependent Schrödinger equation using potential energy curves based on *ab initio* electronic structure calculations as described in our previous work [24, 47]. This model includes both vibrational dynamics in one dimension (CH_2 wagging mode), as well as nonadiabatic coupling between the multiple intermediate neutral states [48]. The simulations are performed using laser parameters (intensity, central frequency, and pulse duration) based on experimental values. A pair of 10-fs pulses with a probe pulse 80% the amplitude of the pump pulse and a peak intensity of 12 TW/cm^2 are used. For simplicity, the multiphoton coupling between the ground state and R_0 and R_3 are set to 0 so that only R_1 is coupled to the ground state, as suggested by our earlier measurements.

Figure 5 shows the results of the simulation in comparison with the experimental data. The experimental PES at each time delay are integrated over the shaded energy regions of Fig. 4, resulting in a yield for each ionic state. Then the yield for each state is divided by the total yield for each delay. Each curve is then normalized to its maximum for comparison. The final populations on the various ionic states are plotted in top of Fig. 5 to compare to the experimental data. These populations are the yields of emitted electrons, corresponding

ion coincidence measurements [46]. The expected energies of the photoelectrons can be found from the energy conservation equation

$$E_{\mathrm{kin}} = n\hbar\nu - I_p - U_p, \quad (2)$$

to the different ionic states in which the molecule is left behind.

The simulation and data show qualitatively similar results. Initially, the dominant contribution to the photoelectron yield is from ionization to D_1, followed by D_3 and then D_0. The yield of

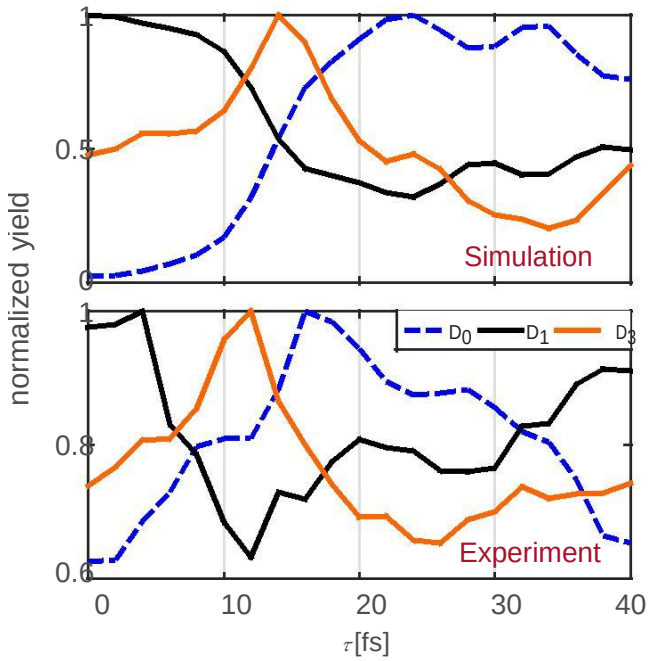

FIG. 5. Normalized yields for ionic states D_0, D_1, and D_3 for a pair of 10-fs pulses with probe amplitude of 80% of the pump for central frequency ω_0 = 402 THz. (Top) Simulation results. (Bottom) Experimental results. Note that the y axis is different from the simulation due to background electrons.

D_1 is decreasing in both simulation and experiment, while the yields of D_3 and D_0 are increasing. In the simulation, there is a peak in the D_3 yield at 14 fs and in the D_0 at 23 fs. These peaks occur at slightly later times than the experimentally measured 12 fs for D_3 and 16 fs for D_0. Both figures show a relatively sharp peak for D_3 and a broader, long-lived peak for D_0. This agreement with experiment confirms our interpretation of the internal conversion dynamics and indicates that, indeed, the measurements are able to separate excitation and ionization and the nonadiabatic molecular dynamics in between.

VI. CONCLUSION

In conclusion, we followed nonadiabatic molecular dynam-ics involved in strong-field molecular ionization by making use of a pump-probe pulse pair produced by an ultrafast optical pulse shaper. Our measurements confirm that nonadiabatic dynamics can play an important role in strong-field molecular ionization which involves intermediate resonances and can lead to the production of multiple states of the molecular cation.

ACKNOWLEDGMENTS

This work has been supported by the National Science Foundation under Award No. 1505679. Support from the European XLIC COST Action CM1204 is also acknowledged.

[1] P. Agostini and L. F. DiMauro, Rep. Prog. Phys. **67**, 813 (2004).
[2] F. Krausz and M. Ivanov, Rev. Mod. Phys. **81**, 163 (2009).
[3] S. Haessler, J. Caillat, W. Boutu, C. Giovanetti-Teixeira, T. Ruchon, T. Auguste, Z. Diveki, P. Breger, A. Maquet, B. Carré *et al.*, Nat. Phys. **6**, 200 (2010).
[4] H. J. Wörner, J. B. Bertrand, P. Hockett, P. B. Corkum, and D. M. Villeneuve, Phys. Rev. Lett. **104**, 233904 (2010).
[5] M. Nisoli, P. Decleva, F. Calegari, A. Palacios, and F. Martín, Chem. Rev. (2017).
[6] H. Niikura, F. Légaré, R. Hasbani, A. Bandrauk, M. Y. Ivanov, D. Villeneuve, and P. Corkum, Nature (London) **417**, 917 (2002).
[7] H. Niikura, F. Légaré, R. Hasbani, M. Y. Ivanov, D. Villeneuve, and P. Corkum, Nature (London) **421**, 826 (2003).
[8] O. Smirnova, S. Patchkovskii, Y. Mairesse, N. Dudovich, and M. Y. Ivanov, Proc. Natl. Acad. Sci. USA **106**, 16556 (2009).
[9] T. Okino, Y. Furukawa, Y. Nabekawa, S. Miyabe, A. A. Eilanlou, E. J. Takahashi, K. Yamanouchi, and K. Midorikawa, Sci. Adv. **1**, e1500356 (2015).
[10] C. Trallero-Herrero and T. C. Weinacht, Phys. Rev. A **75**, 063401 (2007).
[11] H. Maeda, J. H. Gurian, and T. F. Gallagher, Phys. Rev. A **83**, 033416 (2011).
[12] W. D. M. Lunden, P. Sándor, T. C. Weinacht, and T. Rozgonyi, Phys. Rev. A **89**, 053403 (2014).
[13] G. N. Gibson, R. R. Freeman, T. J. Mcllrath, and H. G. Muller, Phys. Rev. A **49**, 3870 (1994).
[14] R. R. Freeman, P. H. Bucksbaum, H. Milchberg, S. Darack, D. Schumacher, and M. E. Geusic, Phys. Rev. Lett. **59**, 1092 (1987).
[15] G. N. Gibson, R. R. Freeman, and T. J. Mcllrath, Phys. Rev. Lett. **69**, 1904 (1992).
[16] R. R. Freeman and P. H. Bucksbaum, J. Phys. B: At., Mol. Opt. Phys. **24**, 325 (1991).
[17] M. Lezius, V. Blanchet, D. M. Rayner, D. M. Villeneuve, A. Stolow, and M. Y. Ivanov, Phys. Rev. Lett. **86**, 51 (2001).
[18] C. Meier and V. Engel, Phys. Chem. Chem. Phys. **4**, 5014 (2002).
[19] D. Mathur and F. A. Rajgara, J. Chem. Phys. **124**, 194308 (2006).
[20] P. Marquetand, M. Richter, J. González-Vázquez, I. Sola, and L. González, Faraday Discuss. **153**, 261 (2011).
[21] F. Lépine, M. Y. Ivanov, and M. J. Vrakking, Nat. Photonics **8**, 195 (2014).
[22] A. Stolow, Annu. Rev. Phys. Chem. **54**, 89 (2003).
[23] A. Stolow, A. E. Bragg, and D. M. Neumark, Chem. Rev. (Washington, DC, US) **104**, 1719 (2004).
[24] P. Sándor, V. Tagliamonti, A. Zhao, T. Rozgonyi, M. Ruckenbauer, P. Marquetand, and T. Weinacht, Phys. Rev. Lett. **116**, 063002 (2016).
[25] By Dyson correlation we refer here to the norm of the Dyson orbital, which is a one-electron function formed by taking a projection of an N-1 electron ionic wave function onto the N-electron wave function of the neutral molecule. A neutral and ionic state are correlated if the norm of this Dyson orbital is large, corresponding to electronic states which have very similar electronic configurations.
[26] C. M. Oana and A. I. Krylov, J. Chem. Phys. **127**, 234106 (2007).
[27] M. Kotur, C. Zhou, S. Matsika, S. Patchkovskii, M. Spanner, and T. C. Weinacht, Phys. Rev. Lett. **109**, 203007 (2012).

[28] M. Spanner, S. Patchkovskii, C. Zhou, S. Matsika, M. Kotur, and T. C. Weinacht, Phys. Rev. A **86**, 053406 (2012).

[29] V. Tagliamonti, P. Sándor, A. Zhao, T. Rozgonyi, P. Marquetand, and T. Weinacht, Phys. Rev. A **93**, 051401 (2016).

[30] J. González-Vázquez, L. González, S. R. Nichols, T. C. Weinacht, and T. Rozgonyi, Phys. Chem. Chem. Phys. **12**, 14203 (2010).

[31] http://learnrnd.com/detail.php?id=Types_of_Acne_and_Long_Term_Effects_of_Acne

[32] P. Sándor, Strong field molecular ionization viewed with photoelectron velocity map imaging, Ph.D. thesis, Stony Brook University, 2016.

[33] M. A. Dugan, J. X. Tull, and W. S. Warren, J. Opt. Soc. Am. B **14**, 2348 (1997).

[34] D. Geißler, T. Rozgonyi, J. González-Vázquez, L. González, P. Marquetand, and T. C. Weinacht, Phys. Rev. A **84**, 053422 (2011).

[35] G. Stibenz, N. Zhavoronkov, and G. Steinmeyer, Opt. Lett. **31**, 274 (2006).

[36] C. W. Hillegas, J. X. Tull, D. Goswami, D. Strickland, and W. S. Warren, Opt. Lett. **19**, 737 (1994).

[37] B. Xu, J. M. Gunn, J. M. D. Cruz, V. V. Lozovoy, and M. Dantus, J. Opt. Soc. Am. B **23**, 750 (2006).

[38] B. Xu, Y. Coello, V. V. Lozovoy, D. A. Harris, and M. Dantus, Opt. Express **14**, 10939 (2006).

[39] V. V. Lozovoy, B. Xu, Y. Coello, and M. Dantus, Opt. Express **16**, 592 (2008).

[40] H. Wang, Y. Wu, C. Li, H. Mashiko, S. Gilbertson, and Z. Chang, Opt. Express **16**, 14448 (2008).

[41] Y. Coello, V. V. Lozovoy, T. C. Gunaratne, B. Xu, I. Borukhovich, C.-h. Tseng, T. Weinacht, and M. Dantus, J. Opt. Soc. Am. B **25**, A140 (2008).

[42] A. T. Eppink and D. H. Parker, Rev. Sci. Instrum. **68**, 3477 (1997).

[43] V. Dribinski, A. Ossadtchi, V. A. Mandelshtam, and H. Reisler, Rev. Sci. Instrum. **73**, 2634 (2002).

[44] A. Zhao, P. Sándor, and T. Weinacht, J. Chem. Phys. **147**, 013922 (2017).

[45] A. M. Weiner, Opt. Commun. **284**, 3669 (2011).

[46] P. Sándor, A. Zhao, T. Rozgonyi, and T. Weinacht, J. Phys. B: At., Mol. Opt. Phys. **47**, 124021 (2014).

[47] J. Finley, P.-A. Malmqvist, B. O. Roos, and L. Serrano-Andrés, Chem. Phys. Lett. **288**, 299 (1998).

[48] The couplings between the crossing diabatic states R_1/R_3 and R_3/R_0 were modeled by Gaussian functions centered at the intersection points C_1 and C_2, respectively. Each coupling term had a full width at half maximum of 0.6 au and an amplitude of 0.082 eV. This coupling amplitude is roughly half of the frequency of the mode investigated, consistent with the presented diabatic picture

http://learnrnd.com/detail.php?id=Data_Storage_in_Liquid_and_Water:Harvard_University_Research